

# Structure and growth morphology of an archetypal system for organic epitaxy: PTCDA on Ag(111)

B. Krause,<sup>1</sup> A. C. Dürr,<sup>1</sup> K. Ritley,<sup>1</sup> F. Schreiber,<sup>1,2,\*</sup> H. Dosch,<sup>1,2</sup>, and D. Smilgies<sup>3</sup>

<sup>1</sup>Max-Planck-Institut für Metallforschung, Heisenbergstrasse 3, D-70569 Stuttgart, Germany

<sup>2</sup>Institut für Theoretische und Angewandte Physik, Universität Stuttgart, Pfaffenwaldring 57, D-70550 Stuttgart, Germany

<sup>3</sup>European Synchrotron Radiation Facility, B. P. 200, F-38043 Grenoble-Cedex, France

(Received 19 March 2002; revised manuscript received 24 July 2002; published 10 December 2002)

The planar organic molecule 3,4,9,10-perylenetetracarboxylic dianhydride (PTCDA) deposited on Ag(111) has been used as a model system for organic molecular-beam epitaxy (OMBE). The crystal structure and morphology of thin films in the range of 50–200 Å have been examined in detail as a function of the growth parameters by x-ray diffraction and noncontact atomic force microscopy. Evidence for the coexistence of  $\alpha$ - and  $\beta$ -like structures has been found for a variety of growth conditions. A growth temperature-dependent morphology transition from smooth films to well-separated islands has been observed which can be related to changes of the crystal structure. These changes of the crystal structure can be rationalized similar to the Nishiyama-Wassermann and the Kurdjumov-Sachs relations. The island density and size show a similar temperature-dependent behavior as observed for MBE-grown inorganic thin films. A rate-equation-based analysis is used to estimate an effective diffusion barrier for the surface self-diffusion of PTCDA.

DOI: 10.1103/PhysRevB.66.235404

PACS number(s): 68.55.Jk, 68.55.Ac, 81.10.Aj, 61.66.Hq

## I. INTRODUCTION

Over the last few years, organic semiconductors have experienced a tremendous increase in research activity, and their attractive electronic and optical properties have become evident.<sup>1</sup> While several device structures have been successfully demonstrated, it has also become clear that, similar to inorganic semiconductors, the exploitation of the full potential of these materials requires a thorough characterization of their structure.<sup>2</sup> Due to the complexity of the organic materials, which is related to their usually low-symmetry crystal structures and their polymorphism, the mechanisms of the structure formation and the resulting morphologies are far from being well understood.

Due to the large number of interesting organic compounds, it is necessary to concentrate the scientific effort on specific model systems, with the aim of developing a complete understanding of the underlying fundamental physics. Of special interest are planar molecules including perylene and pentacene derivatives, phthalocyanines, and other aromatic hydrocarbons such as coronene.<sup>3–5</sup> The comparatively low molecular weight of these molecules in addition to their stability against polymerization and thermal decomposition up to several hundred degrees Celsius allows the controlled deposition of crystalline thin films by organic molecular-beam epitaxy (OMBE).<sup>1</sup> For this class of organic molecules the perylene derivative PTCDA (3,4,9,10-perylenetetracarboxylic dianhydride,  $C_{24}H_8O_6$ , schematically shown in Fig. 1) serves as a model system.<sup>6–9</sup> Moreover, PTCDA has interesting electronic and optical properties with strong anisotropies associated with the crystal structure.<sup>1,10</sup>

The growth of PTCDA multilayers is of particular importance, since many interesting optical, optoelectronic, and electronic properties can only be exploited using high-quality thin films for the design of devices such as organic light-emitting devices, transistors, or waveguides. Several studies of PTCDA multilayers on a variety of substrates have shown the complex and manifold structures of PTCDA thin films

grown on weakly interacting substrates such as KCl, highly oriented pyrolytic graphite, and organic surfaces of self-assembled monolayers,<sup>1,6,11–13</sup> on strongly interacting substrates such as Si and Ni,<sup>14,15</sup> and on substrates with interactions between these extreme cases, such as Au (Ref. 7) and

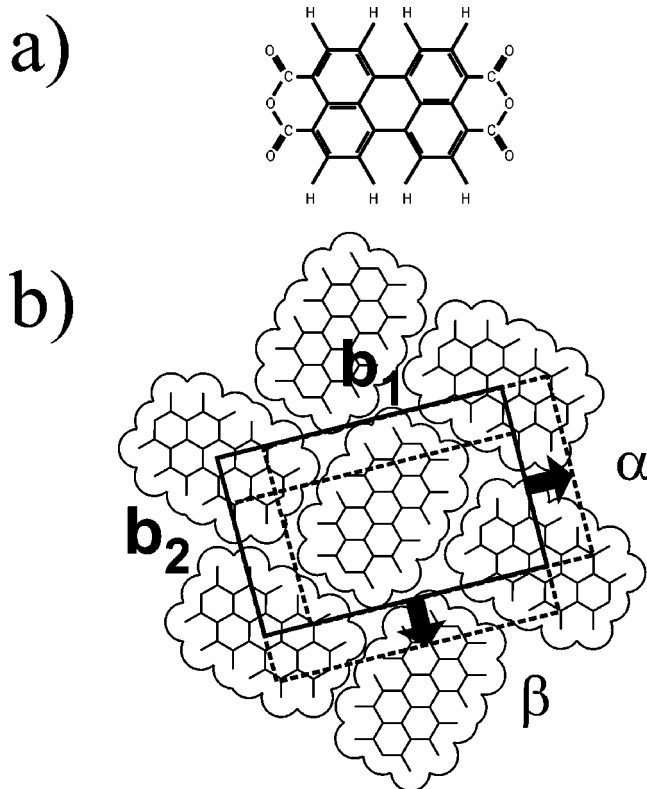


FIG. 1. (a) Structure of the planar PTCDA molecule ( $9.2 \text{ \AA} \times 14.2 \text{ \AA}$ ) consisting of the perylene core (the five central carbon rings) and two anhydride end groups. (b) Schematic of the PTCDA(102) plane. The stacking of the rectangular unit mesh (lattice vectors  $b_1$  and  $b_2$ ) distinguishes  $\alpha$  and  $\beta$  (broken lines: position of the second layer).

Ag.<sup>8,9,16</sup>

The present study is devoted to the structure and growth morphology of PTCDA(102) deposited on a Ag(111) single crystal as a function of the growth temperature,  $T_{\text{growth}}$ , the deposition rate,  $F$ , and the average film thickness,  $d$ . In particular, we address the question of how the thin-film structure is related to the monolayer structure.<sup>9,17</sup> We report results of the growth temperature-dependent crystal structure as studied by grazing incidence x-ray diffraction (GIXD) and the growth temperature-dependent morphology as studied by atomic force microscopy (AFM), optical microscopy, and specular x-ray diffraction. These results are compared with theoretical models for molecular-beam epitaxy (MBE) growth processes. It is shown that, despite the obvious differences between organic-inorganic and metal-on-metal epitaxies, the structure formation exhibits remarkable similarities on the microscopic and mesoscopic scales.

This paper is organized as follows. In Sec. II the experimental procedure is described. The results for the dependence of the morphology and crystal structure on the growth parameters are presented in Sec. III. In Sec. IV, the results are analyzed in detail, and Sec. V contains the conclusions.

## II. EXPERIMENTAL DETAILS

### A. Sample preparation

Bulk PTCDA crystallizes in stacked molecular sheets, each plane containing interlocking PTCDA molecules in a herringbone structure (Fig. 1). Two monoclinic polymorphs have been observed,  $\alpha$  ( $a=3.74$  Å,  $b=11.96$  Å,  $c=17.34$  Å,  $\beta=98.8^\circ$ ) (Refs. 18 and 19) and  $\beta$  ( $a=3.87$  Å,  $b=19.30$  Å,  $c=10.77$  Å,  $\beta=83.6^\circ$ ),<sup>6,20</sup> which differ in the relative stacking of the molecular sheets (See Fig. 1 and Ref. 16).

The PTCDA films studied here have been deposited by OMBE on Ag(111). For all experiments, the same substrate has been used, an Ag(111) single crystal with  $0.23^\circ$  miscut and  $0.15^\circ$  out-of-plane mosaicity.<sup>22</sup> Prior to deposition, the Ag substrate has been cleaned by repeated cycles of sputtering (30 min at room temperature, Ar<sup>+</sup> energy 500–600 eV, Ar pressure  $\approx 6 \times 10^{-5}$  mbar) and annealing at  $\approx 700$ – $900$  K for  $\geq 15$  min. The thoroughly outgassed PTCDA (previously purified by gradient sublimation) has been thermally evaporated from a Knudsen cell. The desired film thickness  $d$  has been monitored by a quartz-crystal microbalance (QCM). In addition, the growth process itself has been monitored in real time by x-ray scattering in a portable MBE chamber.<sup>22</sup>

### B. X-ray and AFM experiments

The AFM experiments have been performed in a stationary OMICRON MBE system. The base pressure of the deposition and analysis chamber is in the  $10^{-11}$  mbar range. The growth chamber is equipped with a quadrupole mass spectrometer, a QCM, and several evaporation cells for organic materials and metals. For the *in situ* analysis of the samples, low-energy electron diffraction (LEED), Auger electron

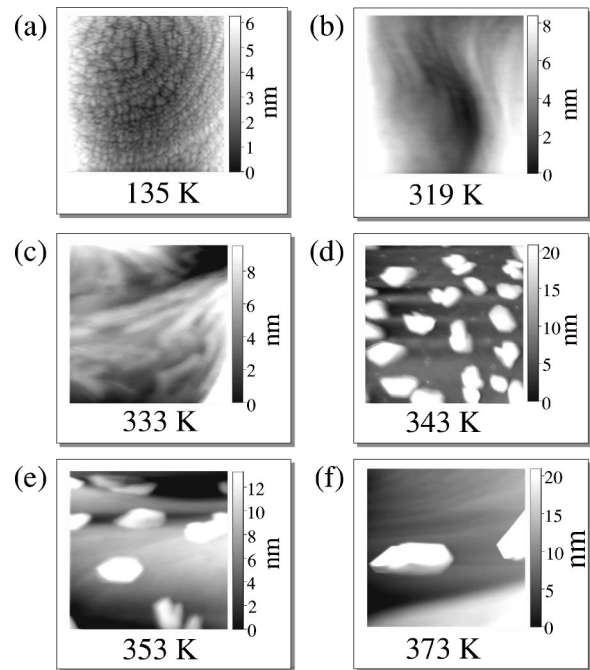


FIG. 2. Morphology of a 50 Å PTCDA film (area  $2.5 \times 2.5 \mu\text{m}^2$ ) as a function of the growth temperature (see main text).

spectroscopy, and a UHV AFM are available. To avoid tip-induced effects on the samples, AFM was done in the non-contact mode.

For the x-ray scattering experiments, a portable, diffractometer-based OMBE chamber has been used, which is described in detail elsewhere.<sup>22</sup> It is a full-featured system for OMBE, but small enough to be mounted directly on a standard diffractometer table. It includes a sputter gun, evaporation sources, a QCM, and installations for sample cooling and heating. A  $360^\circ$  beryllium window permits *in situ*, real-time x-ray-diffraction measurements to be carried out during growth. Pressures in the  $10^{-10}$  mbar range can be achieved with a top-mounted turbomolecular pump and a side-mounted battery-powered ion pump, which maintains the vacuum during transport to a synchrotron-radiation beamline.

The GIXD experiments were performed at beamline ID10B of the European Synchrotron Radiation Facility at a wavelength of  $\lambda=0.932$  Å. Additional experiments were done at  $\lambda=1.237$  Å. The synchrotron experiments were supplemented by measurements at a rotating anode with Mo  $K_\alpha$  radiation.

## III. RESULTS

### A. AFM experiments

In order to study the morphology of PTCDA on Ag(111), a number of films has been grown in the stationary MBE system. They have been deposited at low deposition rates ( $1.3 \pm 0.5$  Å/min) and at substrate temperatures between 135 K and 474 K. The average thickness of the film was  $d=50$  Å for all samples.

Figure 2 shows examples for the different large-scale

morphologies as a function of  $T_{growth}$ . All AFM images are representative, as ensured by measuring several spots of every sample separated by up to several millimeters. For better comparison, the images presented here have identical size of  $2.5 \times 2.5 \mu\text{m}^2$ . At least four separate morphological regions exist: (I) a low-temperature morphology observed at 135 K showing a mesalike structure [Fig. 2(a)], (II) a region characterized by a relatively smooth surface at room temperature [Fig. 2(b)], (III) a transition region at  $333 \pm 5$  K exhibiting facets [Fig. 2(c)], and (IV) a region characterized by crystallites for  $T_{growth} \geq 343$  K [Figs. 2(d)–2(f)]. In the following, these regions will be described in detail.

Region I is characterized by small islands which are arranged along the silver substrate steps. This can be concluded from the characteristic undulation of the island chains which reflects the typical step distribution of the substrate. Perpendicular to the substrate steps the islands are slightly elongated to 100–200 nm. Parallel to the steps the typical width is 50–100 nm. The islands are separated by 0.5–1 nm deep valleys in all directions. They do not appear to be limited by specific facets, but have a smooth, slightly curved surface. Region II reflects the buried silver steps by the presence of lateral waves on a micrometer scale. The single steps change smoothly into one another and cannot be separated. The smooth ripples show a height difference of  $\approx 2$  nm, and sometimes they show a tendency to form more facetlike structures. In the faceted transition region (III) the main facet axis is preferentially aligned parallel to the silver steps. The length of the facets is in the micrometer range. The facets are 100–200 nm wide, and their surfaces are only slightly ( $1^\circ$ – $5^\circ$ ) inclined to the large-scale substrate surface. Most of the islands characterizing region IV are limited on the side by three relatively clear facets and one not-well-defined surface, and on the top by the PTCDA(102) plane.

While for  $T_{growth} > 343$  K only one island size with a certain distribution has been found, for  $T_{growth} = 343$  K small clusters between the crystallites have been observed. The AFM pictures show clearly that the island size (area covered by the islands) increases with temperature from  $\approx 0.1 \mu\text{m}^2$  at 343 K to  $\approx 5 \mu\text{m}^2$  at 413 K, while the island density decreases from  $\approx 12 \mu\text{m}^{-2}$  at 343 K to  $\approx 0.001 \mu\text{m}^{-2}$  at 413 K. The combined analysis of images taken with the optical microscope and the AFM images makes it possible to measure the temperature-dependent changes with statistical significance (see Sec. IV).

## B. X-ray experiments

In order to establish the PTCDA in-plane structure, a large number of Bragg reflections has been measured at a given  $T_{growth}$ . Hyperscripts denote reflections of the  $\alpha$ - or  $\beta$ -type structure, but for consistency the Miller indices are always given in the  $\alpha$  nomenclature.<sup>6,16</sup>

### 1. High-temperature GIXD experiments

Figure 3(a) shows the average in-plane diffraction intensity distribution of the high-temperature sample with  $d = 50$  Å,  $T_{growth} = 448$  K, and  $F = 0.9$  Å/min and its relation

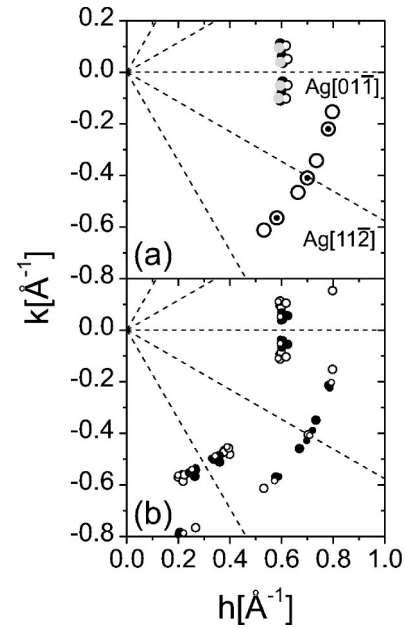


FIG. 3. (a) Position of the measured in-plane intensity distribution of a sample with  $d = 50$  Å,  $T_{growth} = 448$  K, and  $F = 0.9$  Å/min. The crystal orientation of the Ag substrate is indicated to show the epitaxial relation of film and substrate. The reflections have been categorized according to the related bulk polymorph and the reflection type;  $(012)^\alpha$  is represented by large open circles,  $(012)^\beta$  by small black circles,  $(011)^\alpha$  by large black circles,  $(011)^\beta$  by gray circles, and  $(002)^\alpha$  by small open circles (see text). (b) Expected positions of the  $(012)$ ,  $(011)$ , and  $(002)$  reflections (parameters of the unit cell: see text).  $\alpha_1$  is represented by large filled circles,  $\alpha_2$  by small filled circles,  $\beta_1$  by large open circles, and  $\beta_2$  by small open circles.

to the crystal orientation of the substrate. All positions have been determined at the respective growth temperature.

Table I comprises the average  $q$  values of equivalent reflections in comparison with the calculated bulk values. The nomenclature of the measured peaks [Fig. 3(a)] follows from the bulk reflections with the least positional deviations. Since no measurable difference in the  $q$  values of  $(012)$  and  $(01\bar{2})$  has been observed for these films, these reflections are treated as equivalent.

The azimuthal intensity distribution of the  $(012)$  reflections is shown in Fig. 4(a) for two different  $q_z$ . While the azimuthal intensity distribution is relatively broad, the radial in-plane measurements show narrow peaks with an in-plane coherence length of  $550 \pm 100$  Å for all reflections. As an example for the out-of-plane peak width, the raw data of the peaks associated with the  $\alpha$ -like phases around the azimuthal angle  $\phi = 0$  is shown in Fig. 5. The out-of-plane coherence for all measured peaks is  $470 \pm 30$  Å, i.e., higher than  $d$  consistent with the island morphology seen in Figs. 2(d)–2(f).

A thicker, but otherwise similar sample has been grown with  $d = 200$  Å,  $T_{growth} = 453$  K, and  $F = 3.4$  Å/min. In particular, both samples have a similar azimuthal intensity distribution, shown for the  $(012)$  reflections in Fig. 4, and no difference between the  $q$  values of the reflections from both samples could be resolved. Compared to the thin sample, the

TABLE I. Average  $q$  values of the reflections of the high-temperature sample. The reflections have been attributed to the related bulk reflections of  $\alpha$  and  $\beta$  structure. In parentheses: calculated bulk values from the unit-cell dimensions of Ref. 6.

Reflection	$q_z(\text{\AA}^{-1})$		$q_{\parallel}(\text{\AA}^{-1})$		$q(\text{\AA}^{-1})$	
$(012)^\alpha$	0.363	(0.373)	0.911	(0.822)	0.888	(0.902)
$(012)^\beta$	0.309	(0.334)	0.818	(0.824)	0.875	(0.889)
$(011)^\alpha$	0.181	(0.111)	0.605	(0.614)	0.631	(0.641)
$(011)^\beta$	0.298	(0.300)	0.596	(0.601)	0.667	(0.671)
$(002)^\alpha$	0.364	(0.373)	0.624	(0.631)	0.723	(0.733)
$(002)^\beta$		(0.000)		(0.651)		(0.651)

in-plane intensity distribution of the thick sample is more concentrated on specific positions. Measurements of the 200  $\text{\AA}$  sample at room temperature show no significant changes in the azimuthal intensity distribution.

The observed intensity distribution has been attributed to the  $\alpha$  and the  $\beta$  structures, respectively, both with two inequivalent orientations (subscripts 1 and 2).<sup>16</sup> In the upper part of Fig. 4, a schematic of the azimuthal distribution of the peaks and their attribution to the different domains is shown. Table II summarizes the number of domains, the azimuthal separation  $\Delta\phi$  of the  $(012)$  and the  $(01\bar{2})$  reflections, and the epitaxial orientation of the different structures. All in-plane reflections exhibit a characteristic azimuthal asymmetry (Fig. 4) which can be attributed to a rotation of the entire in-plane unit mesh (Sec. IV B). Mirror domains show the same distortion, but in the opposite rotational direction.<sup>16</sup>

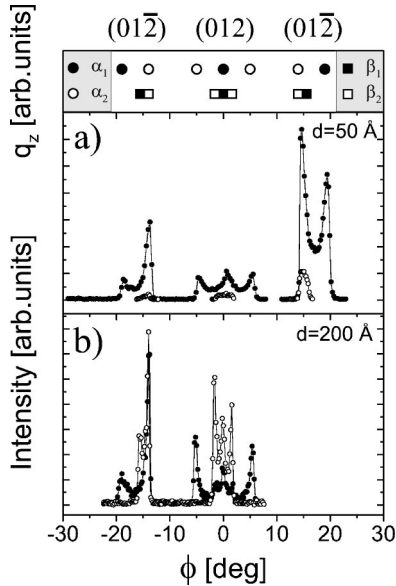


FIG. 4. Azimuthal intensity distribution of the  $(012)$  reflections (the angle  $\phi$  denotes the azimuthal separation to  $\text{Ag}[22\bar{4}]$ ). Atop (a): schematic of the preferential azimuthal positions and their attribution to four structures. The intensity distributions are attributed to  $(01\bar{2})$  and  $(012)$  reflections. Filled circles denote the  $\alpha$ -like structure with higher  $q_z$ , open circles the  $\beta$ -like structure with lower  $q_z$ . (a) Azimuthal intensity distribution of the 50  $\text{\AA}$  sample. (b) Intensity distribution of the 200  $\text{\AA}$  sample. The open circles represent the  $\beta$ -like structure, the filled circles the  $\alpha$ -like structure.

With the assignment of the reflections, and with the model of the rotated domains, the in-plane unit mesh of the preferential  $\alpha$  and  $\beta$  domains has been calculated assuming a rectangular unit mesh, similar to the  $(102)$  plane of the bulk polymorphs. For the  $\alpha$  structure,  $b_1 = 20.11 \pm 0.05 \text{\AA}$ ,  $b_2 = 12.16 \pm 0.05 \text{\AA}$ , and the angle  $\gamma = 90.0 \pm 0.2^\circ$  between  $b_1$  and  $b_2$  have been found. The unit mesh of the  $\beta$  structure has the dimensions  $b_1 = 19.44 \pm 0.05 \text{\AA}$ ,  $b_2 = 12.53 \pm 0.05 \text{\AA}$ , and  $\gamma = 90 \pm 0.2^\circ$ . With these values, the  $(011)$ ,  $(012)$ , and  $(002)$  reflections have been calculated as presented in Fig. 3(b). All measured reflections, i.e., also the  $(011)^\alpha$ , the  $(011)^\beta$ , and the  $(002)^\alpha$  reflections, can be explained consistently which supports the assumption of negligible deviations from a rectangular unit cell (for the thicknesses under investigation). We note that the lattice parameters correspond to the preferential orientation, but a certain distribution of lattice parameters cannot be excluded.

## 2. Low-temperature GIXD experiments

Similar data have been taken for a film with  $d = 50 \text{\AA}$ ,  $T_{\text{growth}} = 318 \text{ K}$ , and  $F = 0.9 \text{\AA}/\text{min}$ . Figure 6(a) shows the measured  $(012)$  reflections in a  $\phi$  range of  $30^\circ$ . The  $(011)$  reflections have been found at  $q_z = 0.18 \text{\AA}^{-1}$ , the  $(012)$  reflections at  $q_z = 0.36 \text{\AA}^{-1}$ . No  $q_z$  splitting of the  $(012)$  intensity distribution could be observed. A scan of the azimuthal intensity distribution of the  $(012)$ -type reflections is shown in Fig. 7(a). While all  $(012)$  peaks are well separated, the  $(011)$

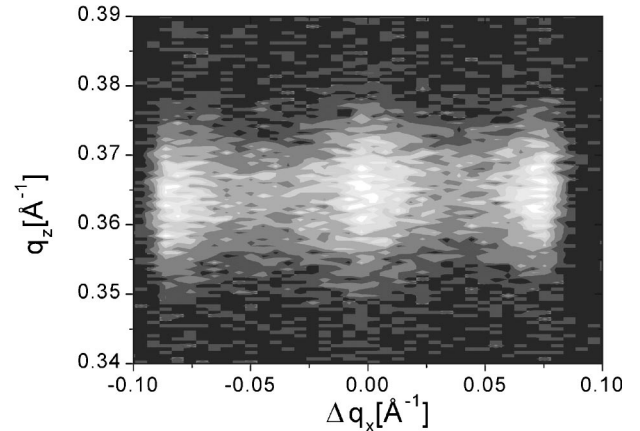


FIG. 5. PSD measurement of the  $(012)^\alpha$  reflections near  $\text{Ag}[22\bar{4}]$ .

TABLE II. Number of azimuthal domains, azimuthal separation of the (012) and the (01 $\bar{2}$ ) reflections, and orientation to the substrate for the PTCDA monolayer (Refs. 9 and 17) and the structures observed in this work for  $T_{growth} = 448$  K (i.e., high  $T_{growth}$ ).

Structure	Domains	$\Delta\phi(^{\circ})$	Alignment
ML	6	13.9	(012) $\parallel$ Ag(22 $\bar{4}$ ) (01 $\bar{2}$ ) $\parallel$ Ag(5 $\bar{7}$ 2)
$\alpha_1$	12	$19.15 \pm 0.3$	(012) $\parallel$ Ag(22 $\bar{4}$ )
$\alpha_2$	12	$19.15 \pm 0.3$	(01 $\bar{2}$ ) $\parallel$ Ag(5 $\bar{7}$ 2)
$\beta_1$	12	$13.9 \pm 0.3$	(012) $\parallel$ Ag(22 $\bar{4}$ )
$\beta_2$	12	$13.9 \pm 0.3$	(01 $\bar{2}$ ) $\parallel$ Ag(5 $\bar{7}$ 2)

reflections consist of two sharp reflections, between which a broad intensity distribution is found. For all reflections, an in-plane coherence length of  $650 \pm 100$  Å and an out-of-plane coherence length of  $50 \pm 5$  Å have been determined.

A thicker ( $d=200$  Å), but otherwise similar, film has been grown at  $T_{growth} = 336$  K and  $F = 3.5$  Å/min. Qualitatively, this film shows the same features as the 50 Å film, as can be seen in Fig. 7(b).

The measured (012)-type reflections can be divided into two groups, according to the intensity and peak width, i.e., sharp and broad reflections. The sharp peaks have been attributed to a  $\beta$ -like structure, the broad peaks to a  $\alpha$ -like structure. The number of domains, the azimuthal separation of the (012) and the (01 $\bar{2}$ ) reflections, and the orientation of the domains to the substrate are summarized in Table III.

Assuming a rectangular unit mesh for both structures [as observed for the (102) plane of the bulk polymorphs], the lattice parameters of  $\alpha$  have been calculated as  $b_1 = 19.8 \pm 0.1$  Å and  $b_2 = 12.2 \pm 0.1$  Å. For  $\beta$ ,  $b_1 = 19.25 \pm 0.05$  Å

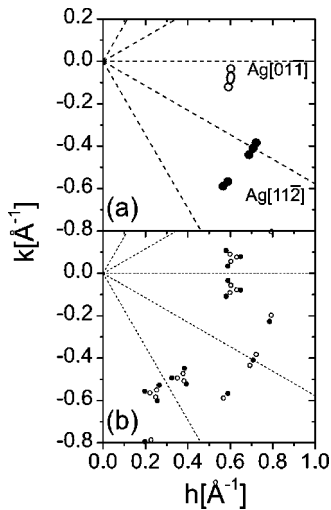


FIG. 6. (a) Positions of the measured in-plane intensity distribution of the sample grown with the parameters  $d=50$  Å,  $T_{growth} = 318$  K, and  $F=3.5$  Å/min. The open symbols denote the (011) peaks, the filled symbols the (012) peaks. (b) Calculated positions of the (011) and (012) reflections of the  $\alpha$  (open circles) and the  $\beta$  (filled circles) structures (for unit-cell dimensions, see text).

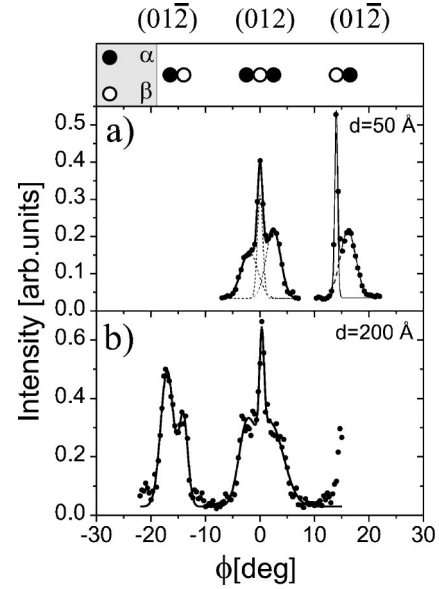


FIG. 7. Azimuthal intensity distribution of the (012)-type reflections. Atop (a) : schematic of the preferential azimuthal positions and their attribution to two structures. The intensity distributions are attributed to (01 $\bar{2}$ ) and (012) reflections. (a) Azimuthal intensity distribution of the 50 Å sample. (b) Intensity distribution of the 200 Å sample.

and  $b_2 = 12.79 \pm 0.05$  Å have been determined. Figure 6(b) shows the simulated reflections, based on the  $b_1$  and  $b_2$  values calculated from the (012) reflections. All measured reflections can be explained with the aligned  $\alpha$ - and the rotated  $\beta$ -like domain sets, yet the positions of the (011) reflections of the  $\beta$ -like structure deviate slightly from the measured value. This may be an indication that either the unit mesh is actually not exactly rectangular for the  $\beta$  structure (which is known to be the case for the monolayer<sup>9</sup>) or the  $q_{\parallel}$  values of the (011)- or (012)-type reflections of  $\alpha$  and  $\beta$  differ slightly.

### 3. Additional GIXD experiments

Several samples have been grown at temperatures between 388 K and 473 K, and at various deposition rates and film thicknesses. In all cases a broad intensity distribution has been observed. As an example, Fig. 8 shows the (012) reflections of a 32 Å sample grown at 473 K. For all samples, a  $q_z$  splitting of the (012)-type reflections has been found, i.e., evidence for the coexistence of the  $\alpha$  and the  $\beta$  struc-

TABLE III. Number of domains, azimuthal separation of the (012) and the (01 $\bar{2}$ ) reflections, and orientation to the substrate for  $T_{growth} = 318$  K (i.e., low  $T_{growth}$ ).

Structure	Domains	$\Delta\phi(^{\circ})$	Alignment
$\alpha$	12	$18.1 \pm 0.5$	(01 $\bar{2}$ ) rotated by $2.2 \pm 0.5^{\circ}$ from Ag(5 $\bar{7}$ 2) to Ag(22 $\bar{4}$ )
$\beta$	12	$13.9 \pm 0.3$	(012) $\parallel$ Ag(22 $\bar{4}$ ) (01 $\bar{2}$ ) $\parallel$ Ag(5 $\bar{7}$ 2)

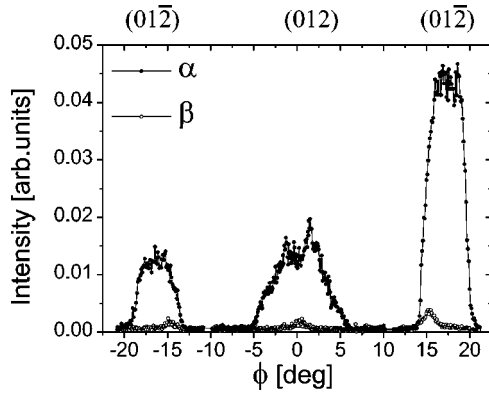


FIG. 8. In-plane intensity distribution of the (012)-type reflections of a sample with the growth parameters  $d=32$  Å,  $T_{growth}=473$  K, and  $F=6.3$  Å/min.

tures. The intensity distribution around  $\phi=0$  has been attributed to the (012), the one around  $\phi=\pm 17^\circ$  to the  $(01\bar{2})$  reflection. While the  $(01\bar{2})$  intensity shows a steep increase at  $\phi=\pm 19^\circ$  and  $\phi=\pm 14^\circ$ , and a constant intensity distribution in between, the (012) intensity distribution is more irregularly distributed in the range of  $\phi=\pm 5^\circ$  and consists of two tips and two shoulders. Most likely, the asymmetric intensity distribution between the peak at  $\phi=17^\circ$  and  $\phi=-17^\circ$  is due to the substrate miscut. The steep decrease of the  $(01\bar{2})$  intensity is found at positions related to the high-temperature structure, while the intensity distribution in between is related to the low-temperature structure. These features, and also the irregular shape of the central peak, can be explained by a superposition of both structures (see Sec. IV B).

#### 4. Coexistence of the $\alpha$ and the $\beta$ polymorphs

The intensity distribution of the in-plane Bragg reflections can be used to determine the ratio of the  $\alpha$ - and the  $\beta$ -like structures. Table IV summarizes the growth conditions and the estimated ratio of the  $\alpha$  and the  $\beta$  structures for several samples. For all samples both structures have been observed. For all samples except one, the  $\alpha$  structure, which is also the preferred bulk structure, dominates. With one exception the  $\alpha$  contribution seems to increase with  $T_{growth}$ . In many cases, the domains aligned to  $\text{Ag}[5\bar{7}2]$ , i.e.,  $\alpha_2$  and  $\beta_2$ , are preferred.

TABLE IV. Estimated ratio of the  $\alpha$  and the  $\beta$  structures. The estimates are made on the basis of the peak intensities of all measured domains. Note, however, that the ratio of  $\alpha$  to  $\beta$  is most likely determined by a very delicate balance of various factors including the morphology and miscut of the substrate.

$T_{growth}$ (K)	$d$ (Å)	$F$ (Å/min)	$\alpha$ (%)	$\alpha_1/\alpha_2$	$\beta$ (%)	$\beta_1/\beta_2$
318	50	0.9	75		25	
336	200	3.5	90		10	
388	180	7	90		10	
448	50	0.9	90	0.5–1	10	1
453	200	3.5	45	0.5	55	0.5
473	32	6.3	95		5	

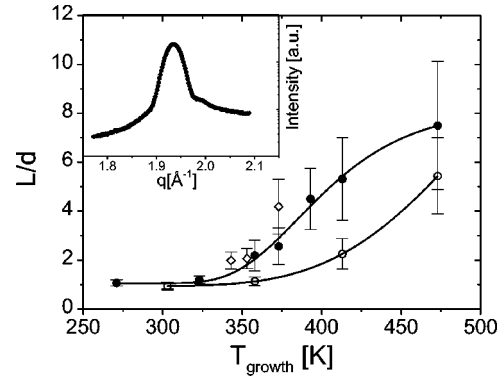


FIG. 9. Growth temperature dependence of the out-of-plane coherence length of two sets of samples with  $d=50$  Å, one grown with  $F=0.8-2.0$  Å/min (filled circles), and the other with  $F=12-14$  Å/min (open circles). The coherence length has been normalized to  $d$ . The open diamonds represent AFM height measurements at similar samples grown with  $F=0.9$  Å/min. The inset shows a typical x-ray scan through the out-of-plane PTCDA(102) reflection ( $T_{growth}=373$  K). The asymmetry of the (102) reflection is related to the distance,  $d_0$ , between the topmost Ag(111) lattice plane and the first PTCDA layer of about 2.9 Å.

#### 5. Out-of-plane measurements

In order to determine the film structure along the surface normal, radial scans through the (102) reflection have been performed. Several samples with  $d=50$  Å/min and with  $F=0.8-2$  Å/min (low  $F$ ) and  $F=12-14$  Å (high  $F$ ), respectively, grown at various  $T_{growth}$ , have been studied.

The temperature dependence of the coherence length  $L$ , as determined from simulations of the measured intensity distribution and normalized to the average film thickness  $d$ , is shown in Fig. 9. For  $T_{growth} \leq 323$  K,  $L$  is constant for the low  $F$  samples and equals  $d=50$  Å. The films are only slightly corrugated at these temperatures. We conclude that the PTCDA crystallites grow coherently from the substrate surface to the film surface. For  $T_{growth} > 323$  K, the coherence length increases strongly, saturating at eight times the average film thickness ( $\approx 400$  Å). In this temperature range, the morphology changes to separate islands, and a comparison with the AFM data shows that the coherence length corresponds to the average island height (Fig. 9). This extends the height measurements to temperatures where the separation between islands is of the order of several micrometers

and therefore too large for statistically significant height measurements with our AFM.

The temperature dependence of  $L$  for the high deposition rate samples is qualitatively similar to the one observed for the low deposition rate samples. For  $T_{growth} \geq 343 \pm 20$  K,  $L$  increases up to several times the average film thickness  $d$ , while for lower temperatures it equals the film thickness. The increase in deposition rate shifts the transition from  $L=d$  to  $L>d$  to higher temperatures.

## IV. DISCUSSION

### A. Morphology

#### 1. Temperature-induced morphology change

As shown above (see, e.g., Fig. 2), we have observed a change from a relatively smooth surface at low temperatures via a facet morphology in an intermediate-temperature range to separate crystallites at high temperatures. For the facets and the smooth film, the diffusion seems to be limited by the substrate steps since the substrate morphology shows a clear imprint of the Ag step structure. At higher temperatures the crystallites extend over the substrate steps. We conclude that there exists a barrier at the Ag step edges which hinders the diffusion at lower temperatures, but may be crossed at  $T_{growth} \geq 343$  K. This is in agreement with scanning-tunneling microscopy (STM) measurements of monolayer coverages where a preferential attachment of PTCDA molecules at step edges has been observed.<sup>9</sup>

The separate islands at higher temperatures are related to Stransky-Krastanov growth, i.e., layer-by-layer growth in the initial monolayers followed by island growth. Details of the layer-by-layer growth of the first monolayers will be discussed elsewhere.<sup>21</sup> The islands show the regular shape of small crystallites and are of similar size. We assume that the measured islands represent the island distribution before they eventually coalesce upon further deposition, since the islands are restricted to a size characteristic for the given growth temperature. Only for  $T_{growth} = 343$  K have two island types (large regular and small irregular islands) been observed. This indicates nucleation at different times, and most likely this sample, grown near the transition temperature to smooth films, does not show the island density before coalescence.

#### 2. Island distribution

In the islanding regime, the island density and size for a constant amount of deposited material vary with  $T_{growth}$ . An inverse relation between the island density  $\rho$  and the island size has been observed. A similar change of island size and density with temperature as observed here has been observed for metal clusters and semiconductor quantum dots.<sup>23–25</sup> In the following, a simple rate-equation model developed in this context will be briefly explained and applied to the PTCDA data.

Nucleation processes increase the number of stable clusters, while the number is decreased by the coalescence. For three-dimensional clusters, it has been found that the maximum cluster density  $\rho$  can be described by

$$\rho \sim \left( \frac{F}{D_{eff}} \right)^p, \quad (4.1)$$

with  $p = i/(i+2.5)$ , the critical cluster size  $i$ , the deposition rate  $F$ , and the effective surface diffusion constant

$$D_{eff} = \nu \exp\left( -\frac{E_{eff}}{k_B T_{growth}} \right). \quad (4.2)$$

$\nu$  is the attempt frequency,  $k_B$  the Boltzmann constant, and  $E_{eff} = E_D + E_i/i$ , where  $E_D$  is the surface diffusion constant and  $E_i$  the nucleation energy of a critical cluster.  $E_{eff}$  approximates  $E_D$  for large  $i$ . If  $\nu$  is independent of  $T_{growth}$ ,

$$\ln(\rho) \sim \text{const} + \frac{pE_{eff}}{k_B T_{growth}}. \quad (4.3)$$

The rate equations used here describe the island densities without referring to any specific property of the islands. Within this model the experimentally determined island density can be directly analyzed. Since the island density and size are related, these data can be used to test the consistency of the above-discussed model. The island density is defined as

$$\rho = \frac{N}{A} = \frac{Nd}{V_{tot}}. \quad (4.4)$$

with the number of the islands  $N$  and the total area  $A$  of the sample. The total volume  $V_{tot} = Ad$  of deposited material is identical for all samples. If a number of wetting layers  $n_{wet}$  (for PTCDA  $n_{wet} \approx 2$ ) with the lattice spacing  $a_{102}$  (i.e., Stransky-Krastanov growth) is taken into account, the effective volume contributing to the islands is  $V^* = V_{tot} - n_{wet} A a_{102}$ .  $V^* = NV$ , where  $V$  is the average volume of an island, and therefore

$$\rho = \frac{1}{V} \sim \frac{1}{L^3}. \quad (4.5)$$

The average volume of an island is defined by three independent vectors with the lengths  $L_1$ ,  $L_2$ , and  $L_3$ . The island size varies monotonously with  $T_{growth}$ , but with a well-defined average shape and aspect ratio, i.e., the ratio of  $L_1$ ,  $L_2$ , and  $L_3$  is temperature independent. Therefore, the average island volume is proportional to  $L^3$  where  $L$  is the length of an arbitrary vector defining the island size.

Assuming Eq. (4.5), the coherence length of the high and low  $F$  data can be analyzed in the same way as the island density determined by AFM. Since  $L^3$  is inversely proportional to  $\rho$ , the slope of  $\ln(L^{-3})$  plotted against the inverse temperature  $1/T_{growth}$  equals  $pE_{eff}/k_B$ . The same analysis, applied to the island area  $A_{island} \sim L^2$ , can be used when plotting  $\ln(A_{island}^{-3/2})$  against the inverse growth temperature.

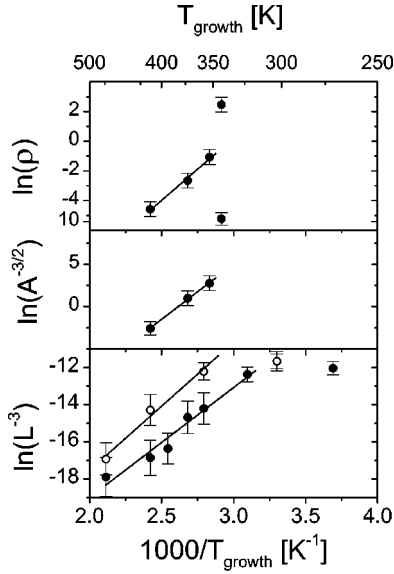


FIG. 10.  $\ln(\rho)$ ,  $\ln(L^{-3})$ , and  $\ln(A^{-2/3})$ , plotted against the inverse growth temperature, using the island density and area determined by microscopic methods, and the island height determined by x-ray diffraction. The gray area indicates growth regime IV. Open symbols refer to a low deposition rate, filled symbols to a high deposition rate.

The above model has been applied to the experimentally determined PTCDA island density, coherence length, and island height (Fig. 10). All plots show a linear behavior for growth temperatures larger than the transition temperature ( $\approx 350$  K) to smooth films. For the island density (excluding the data point at 343 K), and also for the two coherence length data sets, an effective energy barrier  $pE_{eff} = 0.6 \pm 0.2$  eV has been determined. The slope for both coherence length data sets is the same in the island growth temperature range, only the offset varies because of the change in deposition rate. The energy barrier determined from the island area is  $pE_{eff} = 1.1 \pm 0.3$  eV.

The basic assumption for the translation of the island density into the island size is that the islands grown at different  $T_{growth}$  have the same average shape. Since the real shape of the islands can vary to some extent, this assumption is not generally fulfilled. Thus, particularly the results from the geometrical considerations should only be considered as an estimate. Another point is the difference in the statistical sig-

nificance between island height and island area. The island height has been determined by x-ray scattering which averages over large substrate areas, while the microscopy data are restricted to small areas. They can be strongly influenced by the local structure of the substrate. Moreover, it is more difficult to determine the island area than the island density. Therefore, the value estimated from the island density and the island height is more reliable than the value calculated from the island area.

Since PTCDA grows in the Stransky-Krastanov mode, the observed energy barrier, which refers to the later stages of the growth (i.e.,  $d \approx 6 \dots 50$  Å) as opposed to the first monolayers, is an effective energy barrier for surface diffusion of PTCDA on PTCDA. This barrier depends also on the critical cluster size of PTCDA and is a first step for the understanding of the nucleation processes involved in the growth of organic thin films. It is important to note that the diffusion between the islands takes place on the strained wetting layer of PTCDA covering the substrate. A slightly different  $pE_{eff}$  for the growth of PTCDA is expected to be found on a relaxed PTCDA layer with bulk properties.

We emphasize that the energy barriers presented here should be considered only as estimates. Nevertheless, the true value for  $E_D$  will probably lie in the range obtained here. For a more detailed analysis several of the simplifications made here would have to be given up and also a thickness-dependent strain profile could be taken into account. In addition, for the molecules under study, the anisotropy of the interactions would have to be considered at a certain level of refinement.

## B. Epitaxy and strain

In this section the ordering of the PTCDA films on the molecular scale is analyzed, i.e., the crystalline structure of the films and the epitaxial relation to the substrate as derived from the x-ray experiments. Two different types of epitaxially grown PTCDA films have been observed, one for high and one for low  $T_{growth}$ . In Table V, the in-plane lattice parameters and the angle between the neighboring (012) and (01 $\bar{2}$ ) reflections of the bulk structures, the monolayer PTCDA/Ag(111), and the measured high- and low-temperature structures are summarized. In addition, the ratio  $\xi = b_1/b_2$  is shown which is a measure for the distortion of the in-plane unit cell. We now discuss the observed structures in detail.

TABLE V. In-plane unit mesh of the bulk structure, the monolayer structure, and the experimentally determined values for the different structures observed for low and high  $T_{growth}$ .

Structure	$b_1$ (Å)	$b_2$ (Å)	$ \phi(012) - \phi(01\bar{2}) $ (°)	$\xi = b_1/b_2$
Bulk $\alpha^6$	19.91	12.6	19.5	1.665
Bulk $\beta^6$	19.3	12.45	15.8	1.550
Monolayer (Ref. 9)	19.0	12.6	13.9	1.508
$\alpha_1, \alpha_2$ (high $T_{growth}$ )	$20.11 \pm 0.05$	$12.16 \pm 0.05$	$19.15 \pm 0.3$	$1.65 \pm 0.01$
$\beta_1, \beta_2$	$19.44 \pm 0.05$	$12.53 \pm 0.05$	$15.6 \pm 0.3$	$1.55 \pm 0.01$
$\alpha$ (low $T_{growth}$ )	$19.8 \pm 0.1$	$12.2 \pm 0.1$	$18.1 \pm 0.5$	$1.62 \pm 0.02$
$\beta$	$19.25 \pm 0.05$	$12.79 \pm 0.05$	$13.9 \pm 0.3$	$1.50 \pm 0.01$

### 1. High-temperature growth

The in-plane unit mesh of all high-temperature structures is rectangular within the error bar, comparable to the bulk structures. Furthermore,  $\xi_{\alpha}^{exp}$  deviates only by  $0.5 \pm 0.6\%$  from the bulk ratio, and  $\xi_{\beta}^{exp}$  corresponds to the bulk ratio within  $0 \pm 0.6\%$ . We conclude that both structures correspond to a relaxed, but thermally expanded, bulk structure.

The high-temperature structure consists of two  $\alpha$ -like and two  $\beta$ -like structures. All structures are incommensurate with the substrate, the  $\beta_1$  and the  $\alpha_1$  structures are preferentially aligned to  $Ag(22\bar{4})$ , and the  $\beta_2$  and the  $\alpha_2$  structures to a low-symmetry direction of the substrate. We note that, integrated over the film thickness,  $\alpha_1$ ,  $\alpha_2$ ,  $\beta_1$ , and  $\beta_2$  as given in Table V are the dominating structures.

### 2. Low-temperature growth

For low-temperature growth, the unit mesh of the  $\alpha$ -like structure is rectangular, as observed for the bulk unit mesh, while the unit cell of the  $\beta$  structure most likely deviates from this. A deviation from the rectangular unit cell has also been observed for the commensurate monolayer structure investigated in detail in Ref. 9.  $\xi_{\beta}^{exp}$  deviates by at most  $-0.25 \pm 0.6\%$  from  $\xi$  observed for the monolayer, but by  $3.0 \pm 0.6\%$  from the value of the bulk  $\beta$  structure.  $\xi_{\alpha}^{exp}$  is in between the  $\alpha$  and the  $\beta$  bulk values, but is more similar to the  $\alpha$  bulk value with a deviation of  $2.5 \pm 1.2\%$ . We conclude that both structures are incommensurate and distorted relative to the respective bulk structures. The  $\beta$ -like structure is similar to the monolayer structure of PTCDA/ $Ag(111)$ . The  $\alpha$ -like structure corresponds to a distorted  $\alpha$  bulk structure.

The  $\alpha$ -like structure is oriented parallel to the monolayer structure, and the  $\beta$ -like structure is aligned to  $Ag(22\bar{4})$  and the low-symmetry substrate direction, as observed for the monolayer structure. Again we note that, integrated over the film thickness, these are the dominating structures.

### 3. Azimuthal potential

For the high-temperature structure, the intensity distribution in between the preferred orientations of  $\alpha_1$  and  $\alpha_2$ , respectively,  $\beta_1$  and  $\beta_2$ , indicates a rotational distribution of the respective  $\alpha$ -like and  $\beta$ -like domains between the preferential orientations. The azimuthal intensity  $I$  at every orientation corresponds to the number of domains oriented in this direction and can be related to a potential  $U(\phi)$  via  $I \sim \exp[-U(\phi)/k_B T]$ . In Fig. 11, the azimuthal potential, calculated for the  $(01\bar{2})$  intensity distribution between  $\alpha_1$  and  $\alpha_2$  for the sample grown with the parameters  $d=50 \text{ \AA}$  and  $T_{growth}=448 \text{ K}$ , is shown. The two potential minima  $U_1$  and  $U_2$  at the preferred orientations are nearly equivalent. At  $\phi \approx 14^\circ$  and  $\phi \approx 19^\circ$ , a steep potential increase is found. In between these orientations, the potential changes only slightly and assumes a local maximum  $U^+$  at  $\phi \approx 17^\circ$ .  $U^+$  is located at the position of the  $\alpha$ -like structure of the low-temperature structure.

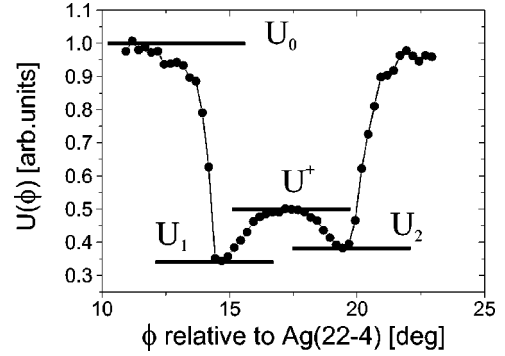


FIG. 11. Azimuthal potential, calculated for the  $(01\bar{2})$  intensity distribution between  $\alpha_1$  and  $\alpha_2$  for the sample grown with the parameters  $d=50 \text{ \AA}$  and  $T_{growth}=448 \text{ K}$ .  $U_1$  and  $U_2$  are the potential minima,  $U^+$  a local maximum, and  $U_0$  the absolute potential maximum.

### 4. Model for the epitaxy

Based on STM and LEED data it was reported that the monolayer PTCDA is commensurate to the substrate and aligned to  $Ag[22\bar{4}]$  and  $Ag[5\bar{7}2]$  with the  $[012]$  and the  $[01\bar{2}]$  directions, respectively.<sup>9</sup> Due to the stronger binding of the monolayer to the substrate, compared to the relatively weak binding between subsequent layers, we do not expect that the commensurate monolayer structure is lifted during further growth. Both reported multilayer structures, the low-temperature and the high-temperature ones, show characteristic orientations related to the monolayer structure.

We propose the following model for the epitaxial growth of a thicker film (at high or low  $T_{growth}$ ) on an initial layer with a monolayer structure. For the low-temperature structure, a strained epitaxial film grows on top of the monolayer structure without changing the orientation of the unit cell, as shown in Fig. 12(a). The directions  $[010]$ , etc., in Fig. 12(a), indicate the in-plane projections of the respective film direction. The  $(010)$  and  $(002)$  planes of monolayer and film are parallel. The orientation of the  $\alpha$ - and the  $\beta$ -like structures is similar. For the high-temperature structure, a relaxed epitaxial film grows on top of the monolayer structure in two orientations for each polymorph, which are both different from the monolayer orientation, as shown in Fig. 12(b). For one orientation, the  $[012]$  directions of the monolayer structure and the film structure are parallel, for the other it is the  $[01\bar{2}]$  directions.

Interestingly, a similar orientational relationship has been observed for the growth of  $fcc(111)/bcc(110)$  in metal epitaxy.<sup>26,27</sup> The  $bcc$  surface structure is rectangular (as is the PTCDA in-plane unit mesh), and the  $fcc$  surface structure hexagonal, but it can also be described by a rectangular unit mesh with the ratio  $\sqrt{3}:1$  between the long and the short sides. In the Nishiyama-Wassermann (NW) orientation, the sides of the rectangular unit cells of  $fcc$  and  $bcc$  are parallel, i.e.,  $fcc(1\bar{1}0) \parallel bcc(001)$ , similar to the observed low-temperature structure of PTCDA/ $Ag(111)$ . In the Kurdjumov-Sachs (KS) orientation, the rectangular unit meshes are aligned along one of the diagonals, i.e., either  $fcc(1\bar{1}0) \parallel bcc(1\bar{1}1)$  or  $bcc(1\bar{1}\bar{1})$ , similar to the high-

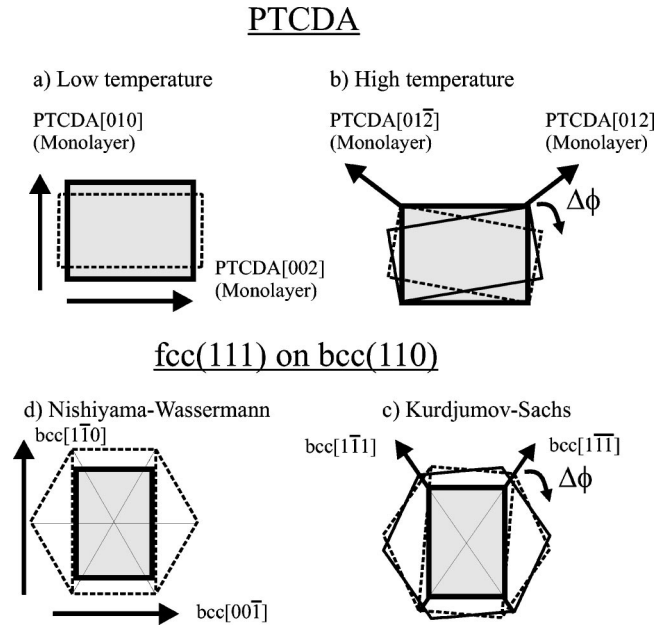


FIG. 12. Orientation of the thin-film unit mesh relative to the template structure (shaded in gray). (a) Orientation of the PTCDA film grown at low  $T_{growth}$  (dashed line) relative to the PTCDA monolayer. The (010) and (002) planes of the monolayer and the film are parallel. (b) Two possible orientations of the PTCDA film grown at high  $T_{growth}$  (dashed and straight thin lines). Either the (012) or the (01 $\bar{2}$ ) planes of the monolayer and the film are parallel. (c) Nishiyama-Wassermann orientation, observed for the growth of fcc(111)/bcc(110) with fcc(1 $\bar{1}0$ )||bcc(001). (d) Kurdjumov-Sachs orientation, observed for the growth of fcc(111)/bcc(110), with fcc(1 $\bar{1}0$ )||bcc(1 $\bar{1}\bar{1}$ ) or bcc(1 $\bar{1}\bar{1}$ ).

temperature orientation of PTCDA/Ag(111). In this context, the calculated azimuthal potential corresponds to the energy of the NW- ( $U^+$ ) and KS-type orientations ( $U_1$  and  $U_2$ ) and their transition region.

For our data, a temperature-dependent transition between a NW- and a KS-type structure can be concluded. For most fcc(111)/bcc(110) systems, only one of the orientations, either KS or NW, has been found since the strain between the unit meshes depends on their size, and therefore also on the ratio of the atomic radii of the substrate and the film. Interestingly, for Pd(111)/Cr(110), a transition from NW to KS via a region where both structures coexist has been observed as a function of  $T_{growth}$ .<sup>26</sup> The coexistence of NW and KS is similar to the superposition of the low- and the high-temperature structures of PTCDA/Ag(111), observed for a variation of growth parameters. Similar to the theoretical predictions for Pd/Cr, the comparison of the strain between [010], [002], and [012] of the relaxed bulk structure of both polymorphs and the commensurate monolayer implies that the KS-type high-temperature structure should be favored in this system. As observed for Pd/Cr, the azimuthal orientations of  $\alpha_1$  and  $\beta_1$  are shifted by 5°, so a large azimuthal shift is not surprising.

The commensurate PTCDA monolayer is strained relative to the bulk polymorphs, which plays an important role for the structural and the morphological transitions. A possible

reason for the temperature dependence of the transition might be that the strain between monolayer and subsequent layers varies due to the different thermal expansion of the substrate and the film. Another aspect is that the films are grown under nonequilibrium conditions. This results in a competition between nonequilibrium and equilibrium structures as a function of  $T_{growth}$ .

It appears that the total energy of the film is minimized by several mechanisms: (i) the structural transition away from the strained monolayer structure, (ii) the evolution of energetically favored facets and separate islands, and (iii) the increase of the volume ratio of the preferred bulk polymorph  $\alpha$  to the less favored  $\beta$  polymorph. We note that the in-plane transition between  $\alpha$  and  $\beta$ , and also the transition from monolayer to bulk structure, correspond only to a slight translational and rotational rearrangement of the molecules.

## V. SUMMARY

We have reported the results of x-ray-diffraction and AFM studies of the structure and growth morphology of thin PTCDA films deposited on Ag(111). Our results provide insight into the complex structure of PTCDA films resulting from the competition between the monolayer and the bulk structures, but also from the competition between the equilibrium structure and the nonequilibrium growth conditions.

The structure formation of thin PTCDA films has been studied in a range of length scales covering several orders of magnitude, from the molecular scale, i.e., the unit-cell dimensions, up to the micrometer scale of the crystallites. From the data, we derived the characteristic temperatures for the morphology changes and the diffusion over substrate step edges, an estimate of the effective energy barrier for surface self-diffusion of PTCDA, and the potential for the orientation of the crystalline structure on top of the monolayer structure.

We could show that many aspects of the organic/inorganic system PTCDA/Ag(111) are similar to the behavior of inorganic molecular-beam epitaxy, despite obvious differences of the systems, such as the lower symmetry of the organic molecule PTCDA compared to metal atoms, the different binding mechanisms in the two systems, and also the size difference between PTCDA and the Ag atoms. The similarities include the concept of the NW and KS orientations, the Stransky-Krastanov growth, and the temperature-dependent island density distribution, which has been analyzed using a simple model developed in the context of inorganic quantum dots.

## ACKNOWLEDGMENTS

We wish to acknowledge useful discussions with N. Karl and H. Port. We are grateful to N. Karl for providing the purified material. Partial support from the DFG (Schwerpunktprogramm ‘‘Organische Feldeffekt-Transistoren’’) is gratefully acknowledged.

- \*Present address: Physical and Theoretical Chemistry Laboratory, University of Oxford, South Parks Road, Oxford OX1, UK.
- <sup>1</sup>S.R. Forrest, *Chem. Rev.* **97**, 1793 (1997).
- <sup>2</sup>D.E. Hooks, T. Fritz, and M.D. Ward, *Adv. Mater.* **13**, 227 (2001).
- <sup>3</sup>N. Karl and C. Günther, *Cryst. Res. Technol.* **34**, 243 (1999).
- <sup>4</sup>E. Umbach, M. Sokolowski, and R. Fink, *Appl. Phys. A: Mater. Sci. Process.* **63**, 565 (1996).
- <sup>5</sup>J.Y. Grand, T. Kunstmann, D. Hoffmann, A. Haas, M. Dietsche, J. Seifritz, and R. Möller, *Surf. Sci.* **366**, 403 (1996).
- <sup>6</sup>M. Möbus, N. Karl, and T. Kobayashi, *J. Cryst. Growth* **116**, 495 (1992).
- <sup>7</sup>P. Fenter, F. Schreiber, L. Zhou, P. Eisenberger, and S.R. Forrest, *Phys. Rev. B* **56**, 3046 (1997).
- <sup>8</sup>C. Seidel, J. Poppensieker, and H. Fuchs, *Surf. Sci.* **408**, 223 (1998).
- <sup>9</sup>K. Glöckler, C. Seidel, A. Soukopp, M. Sokolowski, E. Umbach, M. Böhringer, R. Berndt, and W.-D. Schneider, *Surf. Sci.* **405**, 1 (1998).
- <sup>10</sup>M.I. Alonso, M. Garriga, N. Karl, J.O. Ossó, and F. Schreiber, *Organic Electronics* **3**, 23 (2002).
- <sup>11</sup>D. Schlettwein, A. Back, B. Schilling, T. Fritz, and N.R. Armstrong, *Chem. Mater.* **10**, 601 (1998).
- <sup>12</sup>C. Ludwig, R. Gompf, W. Glatz, J. Petersen, W. Eisenmenger, M. Möbus, U. Zimmermann, and N. Karl, *Z. Phys. B: Condens. Matter* **86**, 397 (1992).
- <sup>13</sup>F. Schreiber, M.C. Gerstenberg, B. Edinger, B. Toperverg, S.R. Forrest, G. Scoles, and H. Dosch, *Physica B* **283**, 75 (2000).
- <sup>14</sup>M. Jung, U. Baston, G. Schnitzler, M. Kaiser, J. Papst, T. Porwol, H.J. Freund, and E. Umbach, *J. Mol. Struct.* **293**, 239 (1993).
- <sup>15</sup>J. Taborski, P. Väterlein, H. Dietz, U. Zimmermann, and E. Umbach, *J. Electron Spectrosc. Relat. Phenom.* **75**, 129 (1995).
- <sup>16</sup>B. Krause, A.C. Dürr, K.A. Ritley, F. Schreiber, H. Dosch, and D. Smilgies, *Appl. Surf. Sci.* **175-176**, 332 (2001). Note that in Eq. (1) of this paper the indices are used differently from here.
- <sup>17</sup>E. Umbach, K. Glöckler, and M. Sokolowski, *Surf. Sci.* **402-404**, 20 (1998).
- <sup>18</sup>A.J. Lovinger, S.R. Forrest, M.L. Kaplan, P.H. Schmidt, and T. Venkatesan, *J. Appl. Phys.* **55**, 476 (1984).
- <sup>19</sup>M. L. Kaplan, C. S. Day, A. J. Lovinger, P. H. Schmidt, and S. R. Forrest (private communication).
- <sup>20</sup>T. Ogawa, K. Kuwamoto, S. Isoda, T. Kobayashi, and N. Karl, *Acta Crystallogr., Sect. B: Struct. Sci.* **55**, 123 (1999).
- <sup>21</sup>B. Krause, F. Schreiber, H. Dosch, A. Pimpinelli, and O.H. Seeck (unpublished).
- <sup>22</sup>K. Ritley, B. Krause, F. Schreiber, and H. Dosch, *Rev. Sci. Instrum.* **72**, 1453 (2001).
- <sup>23</sup>J.A. Venables, G.D.T. Spiller, and M. Hanbücken, *Rep. Prog. Phys.* **47**, 399 (1984).
- <sup>24</sup>J. Johansson, N. Carlsson, and W. Seifert, *Physica E (Amsterdam)* **2**, 667 (1998).
- <sup>25</sup>V.A. Shchukin and D. Bimberg, *Rev. Mod. Phys.* **71**, 1125 (1999).
- <sup>26</sup>O. Hellwig, K. Theis-Bröhl, G. Wilhelmi, A. Stierle, and H. Zabel, *Surf. Sci.* **398**, 379 (1998).
- <sup>27</sup>E. Bauer and J.H. van der Merwe, *Phys. Rev. B* **33**, 3657 (1986).